

# An experimental/theoretical investigation of interfacial instabilities in superposed pressure-driven channel flow of Newtonian and well-characterized viscoelastic fluids

## Part II. Nonlinear stability

B. Khomami<sup>a,\*</sup>, Y. Renardy<sup>b</sup>, K.C. Su<sup>a</sup>, M.A. Clarke<sup>b</sup>

<sup>a</sup> *Department of Chemical Engineering and Materials Research Laboratory, Washington University, St Louis, MO 63130-4899, USA*

<sup>b</sup> *Department of Mathematics, virginia Tech, Blacksburg, VA 24061-0123, USA*

Received in revised form 1 September 1999

---

### Abstract

The interfacial stability of pressure driven channel flow consisting of a highly elastic Boger fluid superposed on as silicone oil is investigated experimentally and theoretically. The viscosity of the two fluids used in the experiments are closely matched, hence any interfacial instability observed in this flow is primarily caused by elastic effects. In Part I of this study (Khomami and Su, 1999) it was demonstrated experimentally and theoretically that this flow system is linearly unstable for a range of depth ratios. In Part II, the dynamics of interfacial waves in the weakly nonlinear regime is examined. Specifically, the Stuart-Landau equation is used to examine the shape of saturated waves. It is shown that the bifurcations are primarily supercritical and the theoretical wave forms compare favorably with experimental measurements. Moreover, it is found that in the weakly nonlinear regime most of the energy transfer occurs between the primary mode and the second harmonic for the fluid system considered. ©2000 Elsevier Science B.V. All rights reserved.

*Keywords:* Interfacial stability; Plane Poiseuille flow; Nonlinear stability; Purely elastic instability

---

### 1. Introduction

Recent experimental investigations into the problem of interfacial instability in superposed channel flow of viscoelastic fluids have been summarized in Part I of this publication [1]. The investigation in Part II is concerned with the nonlinear stability of this class of flows. The linear stability analysis in

---

\* Corresponding author. Tel.: +1-314-935-6065; fax: +1-314-935-7211.

*E-mail address:* bam@poly1.che.wustl.edu (B. Khomami)

Part I predicts the initial growth rate of infinitesimal disturbances. When the disturbance amplitude becomes larger, nonlinear effects enter into the dynamics and either result in subcritical bifurcation with a finite jump to a new solution, or a supercritical bifurcation in which the linear growth saturates to permanent traveling waves. If weak nonlinearities are stabilizing one observes supercritical bifurcations, while subcritical bifurcations are observed when these nonlinearities are destabilizing. To determine the outcome, the Landau constant in the Stuart-Landau equation needs to be calculated [2–4]. Results on longwave evolution such as the Kuramoto-Sivashinsky equation and its generalizations for viscoelastic liquids [5] show that waves with a steep front and gradual tail may result for certain parameter regimes, as well as chaotic interfacial motion. On the other hand, our experimental data are taken at order one wavenumbers. In order to provide information on the order one wavenumbers that have been experimentally observed in [1], we proceed by analyzing the evolution of waves of specific wavenumbers. Using the center manifold reduction technique, the weakly nonlinear interfacial stability of two-layer Newtonian [3,6] as well as superposed flow of upper-convected Maxwell (UCM) fluids have been considered [4]. These studies have shown that the flows bifurcate supercritically over wide parameter ranges, but there is also a sensitivity to the parameters. Subcritical cases include the high viscosity and depth ratios involved in air/water systems. Full numerical simulations using the volume-of-fluid scheme [7,8] have validated linear theory as well as weakly nonlinear theory including saturation for moderate speeds. For very slow speeds, or large initial amplitudes, fingering and migration have been shown to take place [8,9].

The presence of supercritical bifurcations is of great practical interest when the range of convergence of the weakly nonlinear analysis is attainable experimentally and correlate with observations of waves on the interface. A few experimental studies [10–12] have attempted to experimentally investigate interfacial wave shapes in the nonlinear stability regime of superposed plane Poiseuille flows. However, these experiments were conducted with high temperature polymer melts. As a result of the high temperatures and pressures required to process the polymer melts, the investigators were unable to continuously monitor the wave shapes in the nonlinear regime. Hence, the wave shapes, such as the pointed front and gradual tail, were determined by examining the extrudate sample. This resulted in observations which corresponded to the highly nonlinear regime and therefore would not be described by a weakly nonlinear analysis. Moreover since the investigators were unable to continuously monitor the shape of the waves above the saturation amplitude, they were unable to investigate the energy transfer mechanism between the original wave and other frequencies.

As briefly summarized above, only a few studies have had as their focus the nonlinear stability of superposed channel flows. These studies have provided limited results regarding the bifurcation structure of superposed pressure-driven channel flow of viscoelastic fluids. Moreover, all of the above studies have been experimental or theoretical in nature. Hence, the predictive capability of the limited theoretical analyses performed to date has not been examined. In this study, one of our aims is to compare the bifurcation structure and wave shapes predicted by a weakly nonlinear analysis with experiments performed with well-characterized polymeric solutions. Specifically, the purely elastic nonlinear stability of superposed plane Poiseuille flows of viscoelastic fluids as well as the energy transfer mechanism among various disturbances in the nonlinear regime is investigated. Overall, this study contributes to the understanding of purely elastic instabilities, and specifically, the bifurcation that leads to the onset of traveling interfacial waves. The experimental procedure and results are presented in the next section. The details of the mathematical analysis are summarized in the appendices and numerical results for weakly nonlinear waveforms are presented in Section 4. Finally, the conclusions for the study are presented.

## 2. Experimental observations

The experiments were conducted with the Boger fluid system described in Part I [1]. The upper fluid (the Boger fluid) occupies depth  $d_1$  and the lower fluid (silicone oil) occupies depth  $d_2$ . The experimental apparatus and procedure used in this investigation is also the same as that described in detail in Part I. As with Part I, our measurement of interfacial wave positions are made with the aid of digital image processing techniques including the technique for creating composite images. Once the composite images are obtained, their frequency content is examined to see if the frequency obtained from the composite image matches that of the frequency introduced into the system. If this is the case and the wave shapes are sinusoidal, and the growth or decay rates of the interfacial disturbances are exponential, then it is concluded that the flow is in the linear regime. However, if additional frequencies are observed and the growth of interfacial waves are not exponential and the wave shapes are not sinusoidal, it is concluded that the flow is in the nonlinear regime.

To determine the bifurcation structure of the flow, experiments were conducted using pressure pulses that were in the range of 0.5–5% of the channel pressure. Experiments both below the critical as well as above the critical depth ratio were conducted for the Boger fluid/silicone oil system. Below the critical depth ratio (i.e.,  $0.3 \leq d_2/d_1 < 1.0$ , the Boger fluid is in layer 1), we found the interface to be stable irrespective of the amplitude of the initial disturbance. For depth ratios above the critical depth ratio (i.e.,  $1 \leq d_2/d_1 \leq 3$ ), increasing the initial disturbance amplitude generally gave rise to more rapid attainment of the saturation amplitude. In what follows, the results of our experiments in terms of the wave shapes and the frequency content of interfacial disturbances above the critical depth ratio will be discussed.

A number of experiments with the Boger fluid/silicone oil system with initial pressure amplitude of 0.5% of the mean channel pressure have been conducted. As in Part I of this publication, the Reynolds number is defined by  $Re = \rho_1 U_0 d_1 / \eta_1$  and the Weissenberg number  $We = \lambda U_0 / d_1$  (i.e.,  $U_0$  is the velocity at the interface). The experimental range is  $0.0003 \leq Re \leq 0.0004$  and  $2.95 \leq We \leq 6.25$ . For all the experiments conducted, the initial growth rate is observed to be exponential until the saturation amplitude is reached. Once the saturation amplitude is reached the energy associated with the interfacial wave of a given frequency is transferred to other frequencies. As expected, the saturation amplitude varies with the depth ratio and the disturbance wavenumber. In the range of our experiments, the saturation amplitude varies from 0.002 to 0.005 cm. It should be noted that it is very difficult to exactly measure the saturation amplitude based on an exponential fit of the experimental data. Hence, the reported values are the mean values obtained based on three experiments. The standard deviation of the data is  $\pm 18$  to 21%.

Below the saturation amplitude, the interfacial wave is sinusoidal as clearly depicted by Fig. 12 of Part I [1]. However, above this amplitude, the waves are no longer sinusoidal. The reason for this change in shape of the waves is the transfer of energy from the original wave to other frequency waves. Fig. 1 shows typical composite images of interfacial waves above the saturation amplitude. As shown by these composite images, the wave peaks are separated by a larger distance. It should be noted that for a given operating condition the separation distance between the peaks could change significantly as a function of the disturbance frequency (i.e., different dynamics are observed at different disturbance wavenumbers).

To examine the nature of the energy transfer between the introduced disturbances and other frequencies above the saturation amplitude, we have performed a Fourier analysis on the bifurcated waves. It should be noted that we have selected to examine the behavior of the bifurcated waves in this region since we are interested in comparing the experimental results with those of weakly nonlinear analysis. For disturbances with a wavenumber greater than 0.4 the energy associated with the original wave is transferred to higher

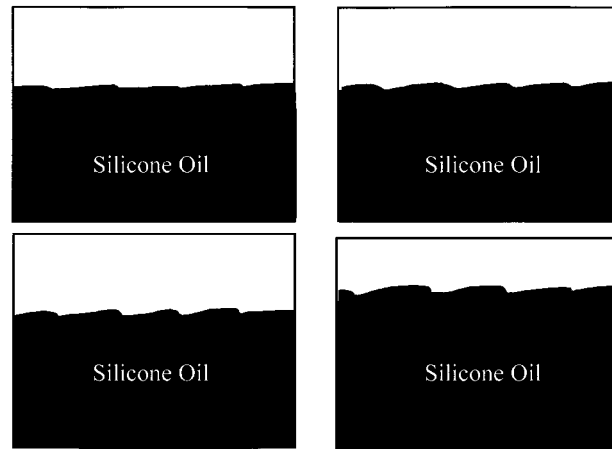


Fig. 1. Representative composite images showing wave amplitude vs. time in the nonlinear regime. Magnification 40–1.

frequencies. In fact, we generally observe most of the energy being transferred to frequencies which correspond to the second harmonic of the original wave frequency. As one moves further from the point where the saturation amplitude is reached, energy transfer to higher frequencies is observed (i.e., 4–6 times the primary frequency), consequently the amplitude of the waves with these higher frequency is rapidly increased. This behavior is consistent with a supercritical bifurcation. However, for wavenumbers smaller than 0.3 we observe a large number of frequencies being excited just above the critical amplitude. In fact, both much larger frequencies than the primary frequency and smaller ones are observed. This type of behavior suggests a subcritical bifurcation.

As the depth ratio is progressively increased above the critical depth ratio the rate of energy transfer from the primary frequency to the second harmonic and higher frequencies becomes more rapid. Hence, the wave shapes in the nonlinear regime begin deviating from the sinusoidal shape in the linear stability regime very quickly. Figs. 2–4 show typical wave shapes in the nonlinear stability regime. Clearly as the depth ratio is progressively increased above the critical depth ratio the wave shapes are observed to deviate significantly from their sinusoidal shape. Moreover, as one moves further away from the point where the saturation amplitude is reached the waves have a much higher frequency content.

### 3. Stability analysis

#### 3.1. Linearized stability of base flow

The full equations governing the weakly nonlinear analysis are given in Appendix A. It should be noted that similar to Part I, the Oldroyd-B Constitutive model which is known to provide a qualitative description of the viscoelastic fluid used in the experiments has been used in the analysis. The computation of growth rates is carried out in Part 1 [1]. We summarize the main points here. In the linearized stability analysis, we discard terms that are quadratic or higher in the perturbations and seek solutions that are periodic in the  $x$ -direction with wavenumber  $\alpha = (2\pi d_1/\text{wavelength})$ ; the perturbation variables are proportional to  $\exp(i\alpha x - i\alpha ct)$ . The growth rate results of Part I are consistent with the independent numerical code of [4]

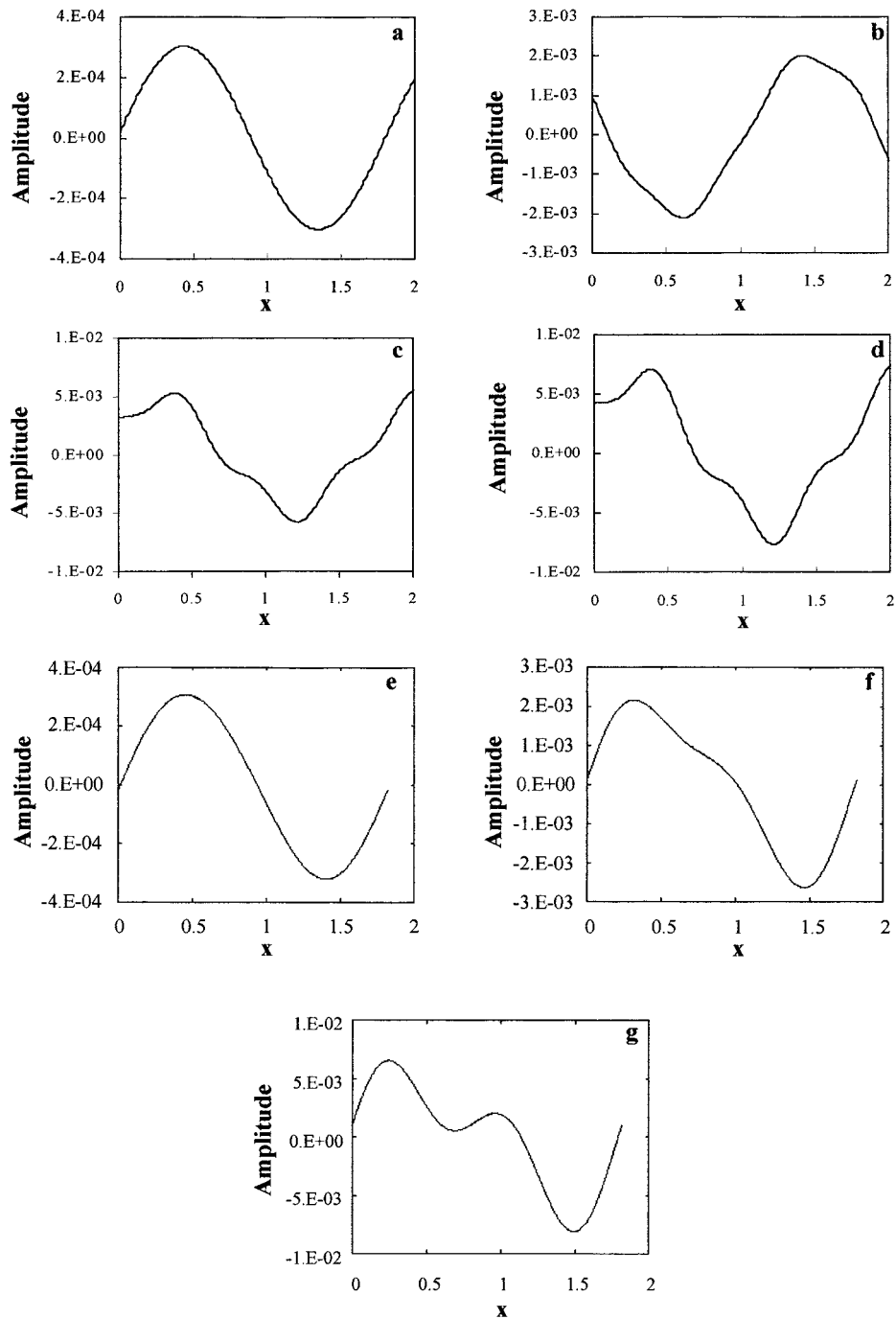


Fig. 2. Experimental and theoretical wave shapes at  $\epsilon = 2.7$ ,  $\alpha = 0.474$ , Interfacial shear rate =  $1.95 \text{ s}^{-1}$ . (a) Observed waveform in the linear regime, 4 in. from inlet, (b) Observed waveform in the weakly nonlinear regime, 4.5 in. from inlet, (c) Observed waveform in the weakly nonlinear regime, 5 in. from inlet, (d) Observed waveform in the nonlinear regime, 6 in. from inlet. Waveforms (e)–(g) predicted by theory. Discussion of theory vs. data is deferred to Section 3.2.

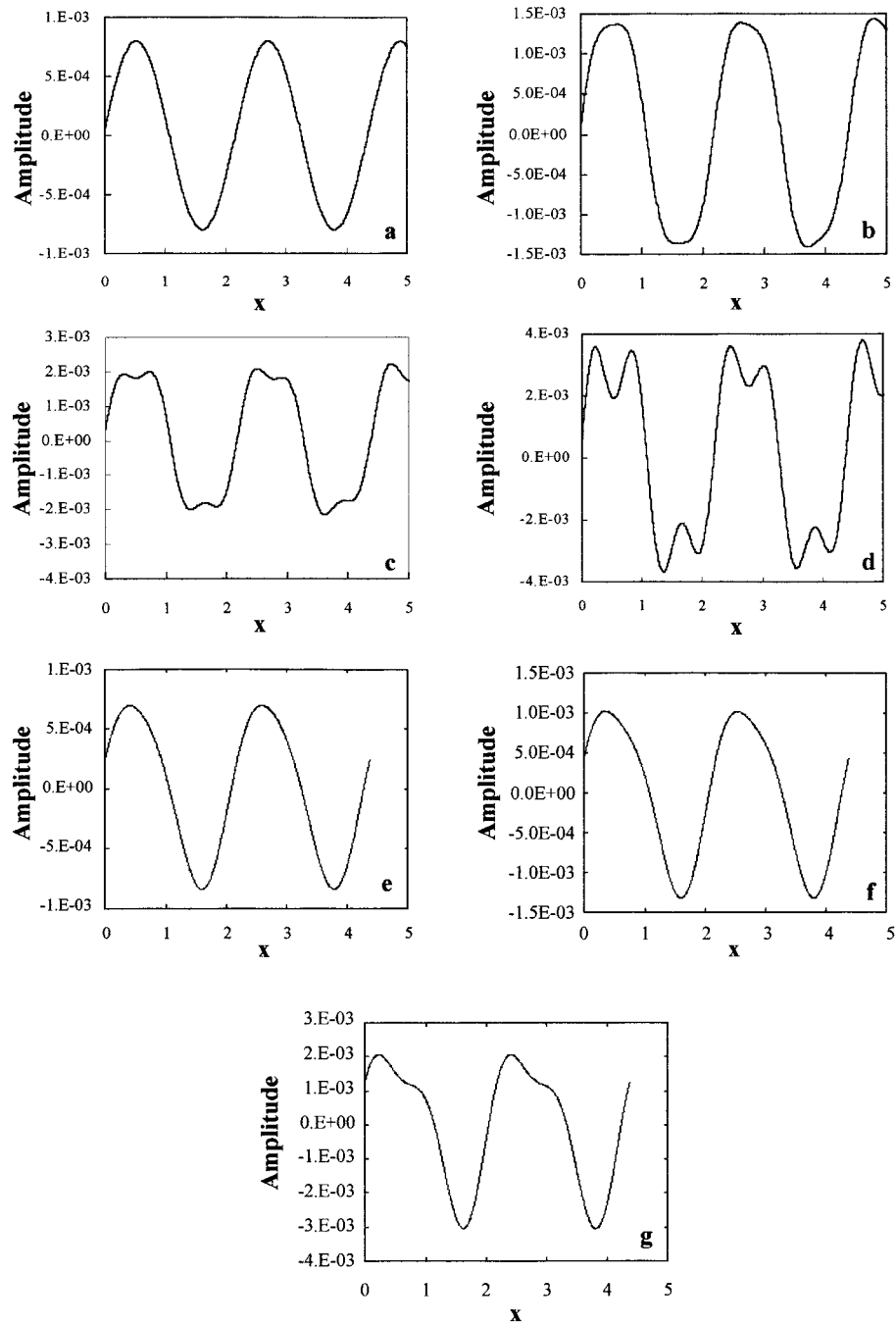


Fig. 3. Experimental and theoretical wave shapes at  $\epsilon = 2.02$ ,  $\alpha = 0.483$ , Interfacial shear rate =  $0.45 \text{ s}^{-1}$  (a) Observed waveform in the linear regime, 5 in. from inlet, (b) Observed waveform in the weakly nonlinear regime, 5.5 in. from inlet, (c) Observed waveform in the weakly nonlinear regime, 6 in. from inlet, (d) Observed waveform in the nonlinear regime, 7.5 in. from inlet. Waveforms (e)–(g) predicted by theory. Discussion of theory vs. data is deferred to Section 3.2.

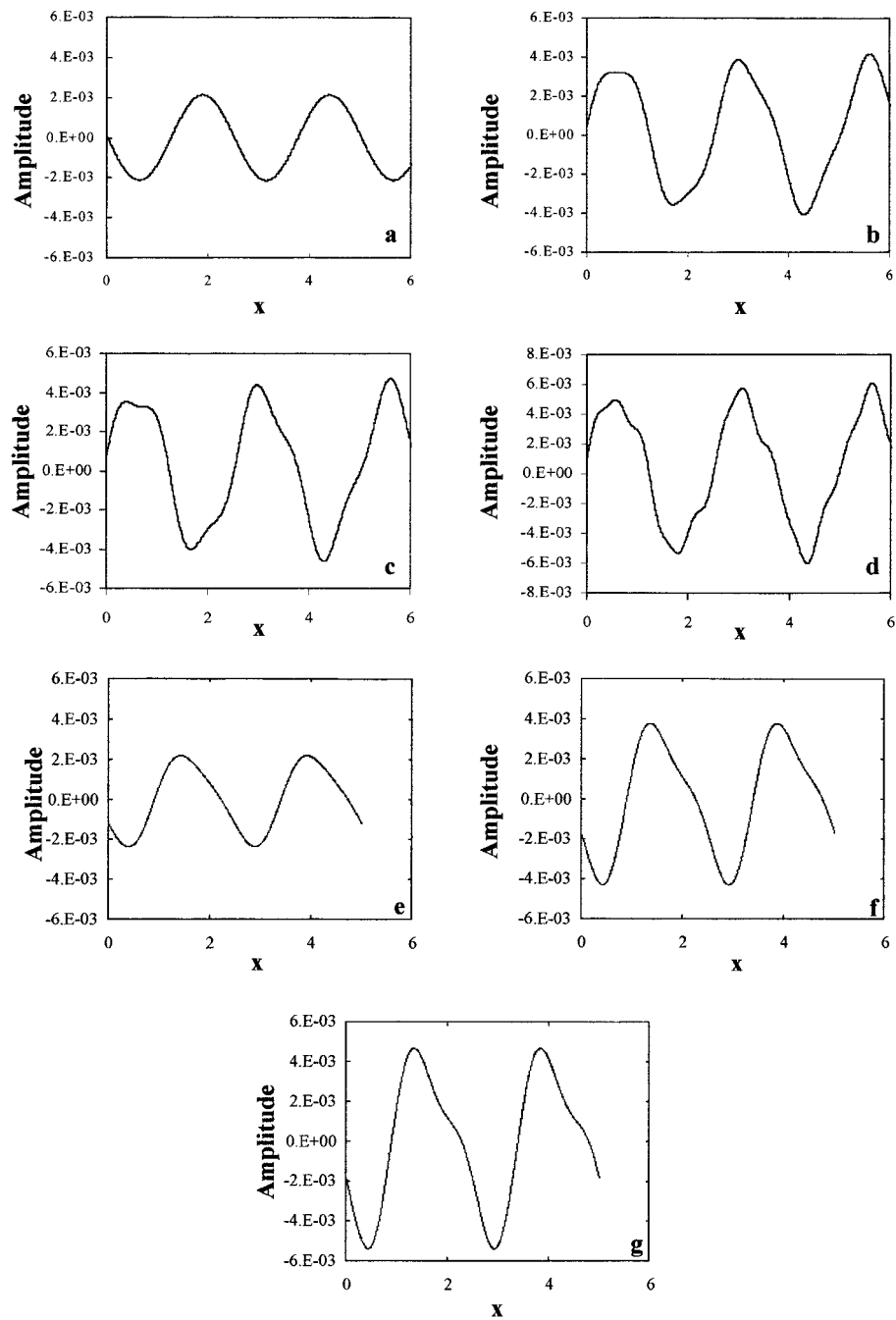


Fig. 4. Experimental and theoretical wave shapes at  $\epsilon = 1.37$ ,  $\alpha = 0.537$ , Interfacial shear rate  $0.45 \text{ s}^{-1}$ , (a) Observed waveform in the linear regime, 6 in. from inlet, (b) Observed waveform in the weakly nonlinear regime, 6.5 in. from inlet, (c) Observed waveform in the weakly nonlinear regime, 7 in. from inlet, (d) Observed waveform in the nonlinear regime, 8.5 in. from inlet. Waveforms (e)–(g) predicted by theory. Discussion of theory vs. data is deferred to Section 3.2.

Table 1

Properties of fluids. Relaxation time  $\lambda$  (s). Density  $\rho$  ( $\text{g cm}^{-3}$ ). Solvent viscosity  $\eta_s$ . Parameter  $\beta = \eta_s/\mu$ ,  $\mu$  denotes total viscosity (poise)

Fluid	$\lambda$	$\rho$	$\mu$	$\beta$
Silicone oil	0	0.908	223	1
Boger fluid	1.7	0.905	234.5	0.84

based on the Chebyshev-tau scheme. This linear code has also been checked against the eigenvalues for Oldroyd-B fluids in [13,14] for the case of zero interfacial tension and equal densities, and the one-fluid results of Tables 1 and 5 of [15].

We have investigated the eigenfunction to determine the major influence of elasticity. The difference between Newtonian liquids and viscoelastic liquids is apparent in the magnitude of the stress perturbation components in the eigenmodes. The dominant variable inducing the instability is the extra stress component  $T_{11}$  in the Boger fluid, followed by the pressure perturbation components in both fluids, then the  $T_{12}$  and  $T_{22}$  stress components in the Boger fluid, then the interface perturbation, and finally the velocity components.

Fluid properties are tabulated in Part I of this publication; however, a number of different viscosity and density silicone oils were considered in Part I. Therefore, Table 1 gives more specifically the values used to calculate waveshapes in Section 3.2. Flow conditions are shown in Table 2. Note that the densities are closely matched and therefore, the influence of gravity is small. The interfacial tension is  $8.5 \text{ dyn cm}^{-1}$ . The growth rates are shown in Fig. 18 of Part I, with instability at depths  $\epsilon = 2.7, 2.02$  and  $1.37$ ; the data with error bars agree favorably with theory for the relevant wavenumbers around  $\alpha = 0.5$ . These are pursued in Section 3.2 below for the weakly nonlinear waveforms.

### 3.2. Bifurcation to traveling wave solution

At the onset of an instability of the base flow, the weakly nonlinear amplitude equation admits a traveling wave solution. This section is concerned with whether the traveling wave solution is linearly stable with respect to perturbations with the same wavenumber as itself. It is then termed a supercritical bifurcation. If on the other hand, the traveling wave solution is unstable, then the bifurcation is termed subcritical. The pressure gradient is kept fixed throughout the nonlinear analysis, as in the experimental situation. In the situation where two-dimensional and three-dimensional modulations or sideband modes are observed (i.e., similar to the experimental observations for disturbances of wavenumber less than 0.3), the theory of [20] applies.

Table 2

Conditions of experiments. Depth fraction  $\epsilon = d_2/d_1$ . Interfacial speed  $U_0$  ( $\text{cm s}^{-1}$ ). Upper fluid depth  $d_1$  (cm)

$\epsilon$	$U_0$	$d_1$	$\lambda_1 U_0/d_1$	$\rho_1 U_0 d_1/\mu_1$
0.844	0.3	0.2755	1.85	0.00032
1.000	0.32	0.2540	2.14	0.00031
1.370	0.34	0.2143	2.70	0.00028
2.020	0.38	0.1682	3.84	0.00025
2.700	0.41	0.1373	5.08	0.00022

The methodology and notation are identical to that of [4]. The details are summarized as follows. Let  $\Phi$  represent the set of unknowns ( $u, v, T_{11}, T_{12}, T_{22}, p, h$ ). The equations and boundary conditions are represented in the schematic form

$$L\Phi = N_2(\Phi, \Phi) + N_3(\Phi, \Phi, \Phi), \tag{1}$$

where the real linear operator  $L$  has the form  $A + Bd/dt$  and  $L(\sigma) = A + \sigma B$ .  $N_2$  contains quadratic terms and  $N_3$  contains cubic terms from the right hand sides of the equations, boundary conditions and interfacial conditions. The components  $f_1, \dots, f_{15}$  of  $N_2 + N_3$  are written in the Appendix of [4] for the upper-convected Maxwell liquid case and are modified here for the Oldroyd-B case. The modifications emanate from the terms involving  $\beta_i$ , namely the base stress components, the Laplacian terms in the momentum equations, terms from the symmetric part of the velocity gradient in the constitutive equations, additional terms in the shear stress balance and the normal stress balance. As in [4], we denote the nonlinearities of the equations of motion in fluid 1 by  $f_1, f_2$ , those of the constitutive equations in fluid 1 by  $f_3, f_4, f_5$ , the corresponding notation for fluid 2 is  $f_6, \dots, f_{10}, f_{11}$  for the continuity of  $u$ ,  $f_{12}$  for the continuity of  $v$ ,  $f_{13}$  for the shear stress balance,  $f_{14}$  for the normal stress balance,  $f_{15}$  for the kinematic condition. We use  $\lambda$  to denote the bifurcation parameter, which can be any of the parameters, e.g. the Reynolds number or Weissenberg number. At  $\lambda = 0$ , there is one eigenvalue, the interfacial mode, at  $\sigma = -ic$ ,  $c > 0$ , for  $\alpha = \alpha_c > 0$  and a corresponding eigenvalue  $\sigma = ic$  for  $\alpha = -\alpha_c$ , and the rest of the eigenvalues are stable ( $\text{Re } \sigma < 0$ ). The eigenfunction with wavenumber  $\alpha$  is denoted by  $\zeta(\lambda)$  and that with wavenumber  $-\alpha$  by  $\bar{\zeta}(\lambda)$ , where the overbar denotes the complex conjugate. For  $\lambda > 0$ ,  $-ic$  becomes  $-s(\lambda)$ . The eigenfunction  $\zeta$  satisfies  $A\zeta(\lambda) = s(\lambda)B\zeta(\lambda)$ . The adjoint eigenfunction with wavenumber  $\alpha$  is denoted by  $b(\lambda)$  and is calculated from the discretized matrix representations of the operators  $A$  and  $B$ , by using the complex conjugate of the transpose of those matrices. The normalization condition is  $(b, B\zeta) = 1$ .  $\zeta$  and  $b$  are proportional to  $\exp(i\alpha x)$ . On the center manifold, the perturbation solution  $\Phi$  can be decomposed as follows

$$\Phi = Z\zeta + \bar{Z}\bar{\zeta} + Z^2\eta + Z\bar{Z}\chi + \bar{Z}Z\chi + \bar{Z}^2\bar{\eta} + \text{higher order terms.} \tag{2}$$

Here, the  $Z(t)$  is the complex-valued amplitude function,  $\chi$  represents the distortion to the mean flow and  $\eta$  is the second harmonic:  $(A - 2s(0)B)\eta = N_2(\zeta, \zeta)$  where  $\eta$  is proportional to  $\exp(2i\alpha_c x)$ . The equation for the mean flow component  $\chi$  simplifies to  $A\chi = N_2(\zeta, \bar{\zeta})$ . Details are given in Appendix B.

The final equation for the amplitude function is

$$\frac{dZ}{dt} + s(\lambda)Z = \kappa|Z|^2Z, \tag{3}$$

$$\kappa = (b, 4N_2(\zeta, \chi) + 2N_2(\bar{\zeta}, \eta) + 3N_3(\zeta, \zeta, \bar{\zeta})). \tag{4}$$

This is the Stuart-Landau equation and  $\kappa$  is the Stuart-Landau coefficient. The purpose of the subsequent numerical work is to calculate  $\kappa$ . If the real part of  $\kappa$  is negative, then the bifurcating solution is supercritical and the traveling wave solution would be stable for small amplitudes. If the real part of  $\kappa$  is positive, then the bifurcating solution would be unstable. When the primary mode interacts with itself and its complex conjugate through the quadratic and cubic nonlinearities in the governing equations, a secondary mean flow mode and a second harmonic are generated. These in turn interact with the primary mode through the quadratic terms, and are balanced with the terms generated by the primary mode interacting with itself in the cubic terms of the equations. The first term in  $\kappa$  arises from an interaction of the primary mode

Table 3

Landau coefficients  $\kappa$  for  $\beta = 0.5$  critical points of one-fluid plane Poiseuille flow. Notation is defined in Appendix A

$R_1$	$W_1$	$\alpha$	$\text{Im}\sigma$	$\kappa$	$\text{Im}\kappa/\text{Re}\kappa$
10334	0.25835	2.1	-0.573	72.70-365.55i	-5.0
8116	1.0145	2.26	-0.664	111.23-412.77i	-3.7

with the secondary mean flow, the second term is an interaction of the primary mode with the second harmonic, and the third term represents a cubic self-interaction.

To reconstruct the nonlinear waveform, we refer to the interface perturbation component in Eq. (2), and use the component  $h$  in the eigenfunction  $\zeta$  and the second harmonic  $\eta$ . We may picture the total interface perturbation as

$$\Phi_h = 2\text{Re}[Z(t)h_\zeta \exp(i\alpha x + i\text{Im}\sigma t) + Z^2(t)h_\eta \exp(2i\alpha x + 2i\text{Im}\sigma t)], \quad (5)$$

where  $Z(t)$  is the amplitude factor. The second harmonic term  $\eta$  contributes  $\sin 2\alpha x$  to the interface shape. The traveling wave solution is predicted to saturate when the real part of the Landau coefficient is negative. When the traveling wave solution is denoted  $Z(t) = \exp(i\omega t)Z_0$  the saturation amplitude is

$$|Z_0| = \sqrt{-\text{Re}\sigma/\text{Re}\kappa}. \quad (6)$$

The present code is constructed from that of [4] for the two-layer Couette-Poiseuille flow of upper convected Maxwell liquids. The results for the Landau constant for fixed pressure gradient for two-layer Couette-Poiseuille flow of Newtonian fluids [3,6] have been checked. In our situation, the flow is pressure-driven Poiseuille flow and the lower fluid is Newtonian. We have also checked (Table 3) against the Landau constants for one-fluid plane Poiseuille flow at the critical points given in Table 5 of [15] at  $\beta = 0.5$ . With the notation of Appendix A, we set  $l_1 = 0.5$ ,  $m = 1$ ,  $w = 1$ ,  $GR_1 = 8$ . The notation of [15],  $(\text{Re}, \alpha, \epsilon, \text{We}, \sigma)$ , corresponds to  $(0.5 R_1, 0.5\alpha, 4W_1/R_1, 2W_1, 0.5\sigma)$  of Appendix A. The value of  $\kappa$  depends on the normalizations for the functions used in the nonlinear analysis, but the ratio of the imaginary to real parts are independent of this. The real part of  $\kappa$  is positive, indicating a subcritical bifurcation. For the Newtonian situation and the upper convected Maxwell liquid [4], the bifurcation is also subcritical.

#### 4. Weakly nonlinear waveforms

For Newtonian flows, predictions of weakly nonlinear theory have been compared with full numerical simulations [8,9]. When growth rates for the interfacial instability are sufficiently large and the amplitudes are small, the saturation predicted by weakly nonlinear theory occurs. It should be noted that in these studies the computations are performed for spatially evolving waves (i.e., similar to the experimentally observed waves) while a temporal weakly nonlinear analysis has been performed. However, as mentioned above a good agreement in terms of waveforms and saturation amplitudes between the numerical simulation and the weakly nonlinear analysis is observed. Considering that a nonlinear version of Gaster's transformation is not available the good agreement between the two predictions suggests that in the weakly nonlinear regime one might be able to use the group velocity to obtain spatial waveforms from a temporal weakly nonlinear analysis. However, we have chosen not to follow this strategy due

Table 4  
Conditions where experimental waveforms were obtained

$\epsilon$	$\alpha$	$\kappa$	$\text{Im}_\kappa/\text{Re}_\kappa$	$h_\zeta$	$h_\eta$
2.7	0.474	-1E-5-6E-6i	0.6	-1E-5-1E-4i	0.1E-5-0.3E-5i
2.02	0.483	-1E-3-2E-3i	1.2	2E-4-7E-4i	9E-5-1E-5i
1.37	0.537	-3E-3-8E-4i	0.25	-5E-3+5E-3i	3E-3+2E-3i

the fact that it is not based on a sound theoretical foundation. Instead, we have chosen to compare the waveforms predicted by the weakly nonlinear analysis with those of the experiments. Clearly one cannot expect the analysis to exactly predict the wave amplitudes, however if the analysis is capable of describing the wave dynamics in the weakly nonlinear regime the relative amplitudes of the fundamental frequency and the overtone as well as the overall waveforms should be predicted with reasonable accuracy.

In what follows, we compare the waveforms predicted by the weakly nonlinear theory with experimental waveforms for the Boger fluid/silicone oil system. The theory of Section 3.2 applies when the amplitude is small for the primary mode, say of wavenumber  $\alpha$ , and this is the only mode to be excited as a bifurcation parameter (such as the applied pressure gradient), is increased. Table 4 shows the Landau coefficients for cases where experimental waveforms were obtained. The dimensionless wavenumber is  $\alpha = (2\pi d_1/\text{wavelength})$  as defined in Part I [1]. The last two columns of Table 4 show the perturbation to the interface height  $h$  for the eigenfunction  $\zeta$  and the second harmonic  $\eta$ . A comparison of these values indicates the strength of excitation of each mode in the weakly nonlinear interaction influences the interface shape. Hence, these terms are utilized in Eq. (5) to reconstruct the nonlinear waveforms plotted in (e)–(g) of Figs. 2–4.

At  $\epsilon = 2.02$  and  $2.7$ , the bifurcation is close to a resonant situation and the analysis yields small Landau coefficients, close to subcritical. There are subcritical bifurcations close by, for smaller wavenumbers in these cases. The resonance is evident through an evaluation of the three nonlinear terms which contribute to the Landau constant in Eq. (4); it is found that the main contribution to  $\kappa$  arises from the interaction of the primary mode with the second harmonic, while the cubic self-interaction term is smaller, and the interaction of the primary mode with the mean flow component is found to be negligible. The importance of the second harmonic is also evident in the experimental data.

There is very good agreement between the experimental waveform in Fig. 2(b) and the theoretical waveform in Fig. 2(f). The higher harmonics affect the wave shape as in (g). The nonlinear waves observed in Fig. 2(d) reflect the strong presence of higher harmonics. The amplitudes are (e)  $|Z(0)| = 2.2$ , (f)  $|Z(0)| = 15$  and at (g), the saturation amplitude  $|Z_0| = 35$  is used. There is also good agreement between the waveforms in Figs. 3 and 4. The observed amplitude is a function of how far away the situation is from a bifurcation point, and whether the wave is close to a saturated state, in addition to the error associated with experimental measurements. These issues along with the approximate nature of the constitutive equation used in the analysis as well as the fact that a temporal analysis is performed while the experimental waves evolve spatially will lead to differences in the quantitative amplitudes; however, the experimental waveforms compare qualitatively well with the waveforms predicted by the weakly nonlinear theory.

#### 4.1. Effect of wavenumber

As evident from Fig. 18 of Part I [1] of this publication, the depth ratio  $\epsilon = 2.7$  exhibits the largest range of unstable wavenumbers and the highest growth rates. The effect on the waveforms of changing

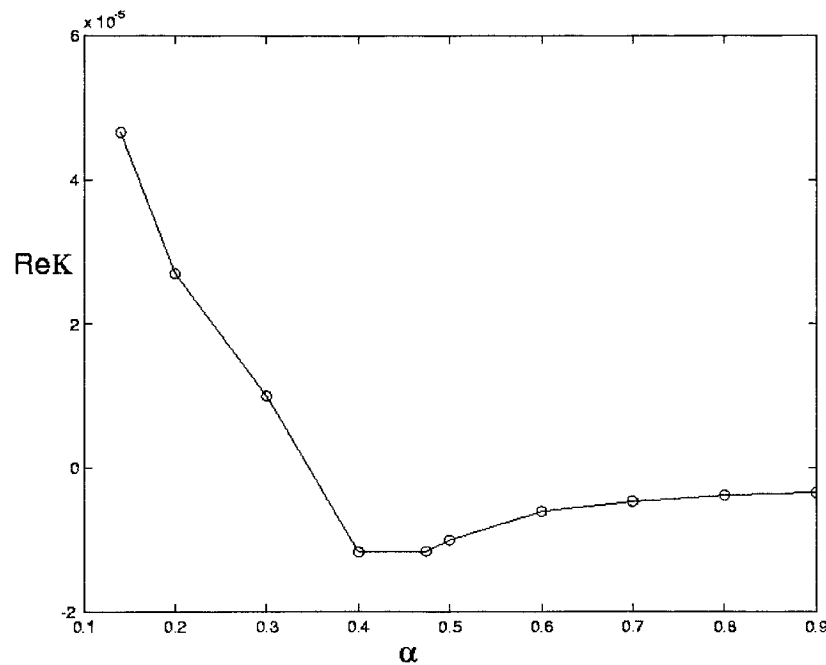


Fig. 5. The influence of wavenumber on the nature of the bifurcation. Depth ratio  $\epsilon = 2.7$ . Wavenumbers are varied below and above 0.474 value where experimental waveforms are shown in Fig. 2.

wavenumbers is examined first at this depth ratio. The unstable wavenumbers range from 0 to 2.9, while the experiments were conducted around 0.5. At the lower end of the wavenumbers, therefore, the weakly nonlinear calculations suffer from resonant interactions with the second harmonic. This situation may occur when the higher harmonics are also excited as primary instabilities and the eigenvalues are multiples of the primary mode. This behavior is consistent with what has been observed experimentally, (i.e., excitation of multiple higher harmonics for wavenumbers lower than 0.3). At resonance, the Landau coefficient  $\kappa$  has a pole, and the vicinity is reflected in the large  $|\text{Im}\kappa/\text{Re}\kappa|$  where it changes sign. Fig. 5 shows the real part of the Landau coefficients and the wavenumbers below 0.3 are subcritical bifurcations, while the wavenumbers above are supercritical bifurcations. The weakly nonlinear waveforms for the maximum growth rate mode at wavenumber 0.9 is shown in Fig. 6. This is qualitatively similar to that of the experimentally observed waves at wavenumber 0.5.

For the depth ratios  $\epsilon = 1.37$  and 2.02, the range of unstable wavenumbers is smaller than the depth ratio 2.7. The maximum growth rate mode and the neutral mode are given in Table 5, showing supercritical bifurcations. The waveforms are qualitatively similar to those of Figs. 3 and 4.

#### 4.2. Influence of densities and interfacial tension

For our Boger fluid system, slight changes in interfacial tension and inclusion or exclusion of gravity do not have an appreciable effect on stability. However, this is due to the fluid properties, namely the densities are similar so that the effect of gravity is small, and the instabilities at the long or order one wavelength are not influenced by interfacial tension as much as they would be for shorter waves. When

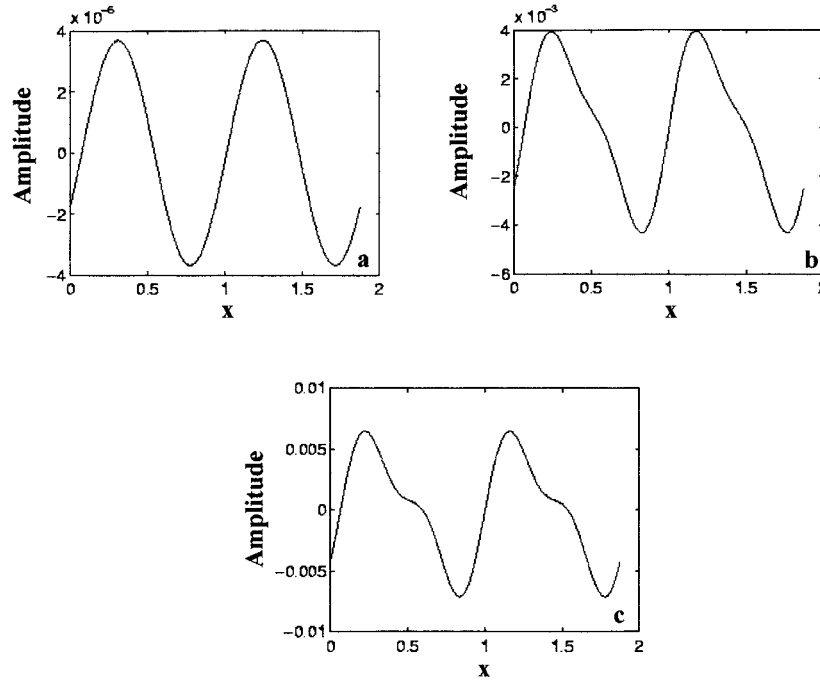


Fig. 6. Waveforms  $\Phi_h$  cm vs. horizontal distance  $x$  cm,  $\epsilon = 2.7$ ,  $\alpha = 0.9$ , maximum growth rate mode.  $\rho_1 = 0.90.5 \text{ g cm}^{-3}$ ,  $\rho_2 = 0.908 \text{ g cm}^{-3}$ . (a) linear, (b) weakly nonlinear, (c) larger amplitude.

these influences are appreciable, the main points of sensitivity arise as follows. Asymptotically for short waves, interfacial tension appears at  $O(\alpha)$  in the growth rate and is stabilizing. For the upper-convected Maxwell liquids [16–18] the competition between viscous and elasticity stratifications appears at  $O(1)$ . As a result of this, the growth rate for zero interfacial tension and gravity asymptotes to a non-zero constant. The  $O(1)$  growth/decay rate for short waves due to elasticity stratification occurs also in the numerical results for the Johnson-Segalman model [19]. The density stratification appears through the inclusion of gravity at  $O(1/\alpha)$ . If the relaxation times of the fluids were zero, then the corresponding growth rates for the purely viscous stratification appears at  $O(1/\alpha^2)$ . The inclusion of elasticity in our case enhances the growth rates over all wavenumbers, thus the viscoelastic instability would be easier to detect than the Newtonian. Also, the elasticity stratification stabilizes the short waves, as well as affecting other wavenumbers.

Table 5

The maximum growth rate mode, followed by a neutral mode, are given for  $\epsilon = 1.37, 2.02$

$\epsilon$	$\alpha$	$\kappa$	$\text{Im}\kappa/\text{Re}\kappa$	$h_\zeta$	$h_\eta$
1.37	0.34	$-0.005 - 0.002i$	0.4	$-0.006 + 0.004i$	$0.007 + 0.007i$
1.37	0.5	$-0.8 + 1i$	-1.3	$0.03 - 0.008i$	$0.7 + 0.15i$
2.02	0.8	$-6E-5 - 2E-5i$	0.4	$-1E-3 - 5E-4i$	$0.2E-6 - E-5i$
2.02	1.3	$-5E-5 + 5E-5i$	-0.9	$-2E-4 - 2E-4i$	$-5E-6 - 4E-6i$

## 5. Conclusions

The dynamics of purely elastic interfacial waves in the nonlinear regime have been examined experimentally and theoretically. The predictions of the weakly nonlinear analysis have been compared with the experimental data and in cases where the linear theory and experiments agree, the weakly nonlinear theory captures the interfacial waveforms, i.e. the location of humps on the peaks and the troughs are accurately predicted. For the Boger fluid system, the theory predicts a strong presence of the second harmonic, with energy transfer from the interaction of the primary mode with itself via quadratic terms in the governing equations. The interaction of the primary mode to form the mean flow component and the cubic selfinteraction are small. These theoretical conclusions compare well with experimental data that shows significant energy transfer to the second harmonic above the saturation amplitude.

## Acknowledgements

This research was sponsored by the National Science Foundation. Y. Renardy acknowledges support under Grant No. CTS-9612308. B. Khomami acknowledges support under Grant Nos. CTS-9304035 and CTS-9840937.

## Appendix A. Governing equations for the weakly non-linear analysis

In this Appendix, we adopt the notation of [2,4]. The notation  $(\alpha, c, (\Lambda_1)_2, (\Lambda_2)_2, \text{Re}, R_m, \epsilon, (\Lambda_1)_2/(\Lambda_1)_1)$  of [13,14] corresponds to our  $(\alpha l_2, \sigma/(-i\alpha), W_1/l_2, \beta_1 W_1/l_2, R_2 l_2, m, l_1/l_2, w)$ . Fluid 2 lies over fluid 1. Densities are denoted  $\rho_i (i = 1, 2)$ , solvent viscosities  $\eta_{si}$ , polymeric viscosities  $\eta_{pi}$ , total viscosities  $\mu_i = \eta_{si} + \eta_{pi}$ , relaxation times  $\lambda_i$ , and  $\beta_i = \eta_{si}/\mu_i$ . The walls are located at  $z^* = 0, l^*$ . Asterisks are used for dimensional variables. The upper plate moves with velocity  $(U_p^*, 0)$  and the bottom plate is at rest. In the basic flow, fluid 1 occupies  $0 \leq z^* \leq l_1^*$  and fluid 2 occupies  $l_1^* \leq z^* \leq l^*$ . The velocity of the interface in the basic flow is  $(U^*(l_1^*), 0)$ . and for brevity, we denote  $U^*(l_1^*)$  by  $U_i$ . The velocity, distance, time and pressure are made dimensionless with respect to  $U_i l^*, l^*/U_i$ , and  $\rho_1 U_i^2$ . The extra stress components are scaled the same as the pressure. In Couette-Poiseuille flow, the basic flow has a pressure gradient  $-G^*$  in the  $x$ -direction. Reynolds numbers in fluid  $i$  are denoted  $R_1 = U_i l^* \rho_1 / \mu_1$  and  $R_2 = U_i l^* \rho_2 / \mu_2$ . Weissenberg numbers are denoted by  $W_1 = U_i \lambda_1 / l^*$  and  $W_2 = U_i \lambda_2 / l^*$ . For Couette-Poiseuille flow, there are 11 dimensionless parameters: a Reynolds number, say  $R_1$ , a Weissenberg number  $W_1$ , the undisturbed depth  $l_1$  of fluid 1, a surface tension parameter  $T = (\text{surface tension coefficient})/(\mu_2 U_i)$ , a Froude number  $F$  given by  $F^2 = U_i^2 / g l^*$  where  $g$  is the gravitational acceleration constant, a dimensionless pressure gradient  $G = G^* l^* / (\rho_1 U_i^2)$ , the viscosity ratio  $m = \mu_1 / \mu_2$ , a density ratio  $r = \rho_1 / \rho_2$ , the ratio of relaxation times  $w = \lambda_1 / \lambda_2 = W_1 / W_2$ , and the parameters  $\beta_1$  and  $\beta_2$ . In this Appendix, we present the equations governing the problem the problem for the general Couette-Poiseuille flow. The momentum equation in dimensional variables is

$$\rho_i \left( \frac{\partial \mathbf{u}^*}{\partial t} + \mathbf{u}^* \cdot \nabla^* \mathbf{u}^* \right) = \nabla^* \cdot \mathbf{T}^* - \nabla^* p^* - \rho g \mathbf{e}_z + \eta_{si} \nabla^{*2} \mathbf{u}^*, \quad (\text{A.1})$$

where the stress tensor is

$$\underline{\tau}^* = -p^* \mathbf{I} + \mathbf{T}^* + \eta_{si} [\nabla^* \mathbf{u}^* + (\nabla^* \mathbf{u}^*)^T], \tag{A.2}$$

$\mathbf{T}^*$  is the extra stress tensor. Asterisks denote dimensional variables (velocity  $\mathbf{u}^*$  and pressure  $p^*$ ).

The dimensional constitutive law for the Oldroyd-B fluid is

$$\mathbf{T}^* + \lambda_i \frac{D\mathbf{T}^*}{Dt^*} = \eta_{pi} (\nabla^* \mathbf{u}^* + (\nabla^* \mathbf{u}^*)^T), \quad \mathbf{u}^* = (u^*, v^*), \tag{A.3}$$

where  $D/Dt^*$  is the upper convected time derivative

$$\frac{D\mathbf{T}^*}{Dt^*} = \frac{\partial \mathbf{T}^*}{\partial t^*} + (\mathbf{u}^* \cdot \nabla^*) \mathbf{T}^* - (\nabla^* \mathbf{u}^*) \mathbf{T}^* - \mathbf{T}^* (\nabla^* \mathbf{u}^*)^T. \tag{A.4}$$

Next, we consider the stress balance. The shear stress condition is

$$[[\mathbf{t} \cdot \underline{\tau} \cdot \mathbf{n}]] = 0 \tag{A.5}$$

where the interface is located at  $z = l_1 + h(x, t)$ , and the unit tangent vector is  $\mathbf{t} = (1, h_x) / \sqrt{1 + h_x^2}$ , the normal  $\mathbf{n} = (-h_x, 1) / \sqrt{1 + h_x^2}$ . The quantities are evaluated at  $z = l_1$ , where

$$\begin{aligned} \tau_{11} &= -P - hP' - \frac{h^2}{2} P'' - p - hp' - \frac{h^2}{2} p'' + C_1 + hC_1' + \frac{h^2}{2} C_1'' + T_{11} + hT_{11}' + \frac{h^2}{2} T_{11}'' \\ &\quad + \left( \frac{\beta_i}{R_1} \right) \left( \frac{\mu_i}{\mu_1} \right) 2 \left( u_x + hu_{xz} + \frac{h^2}{2} u_{xzz} \right), \\ \tau_{12} &= C_2 + hC_2' + T_{12} + hT_{12}' + \frac{h^2}{2} T_{12}'' \\ &\quad + \left( \frac{\beta_i}{R_1} \right) \left( \frac{\mu_i}{\mu_1} \right) \left( u_z + hu_{zz} + \frac{h^2}{2} u_{zzz} + v_x + hv_{xz} + \frac{h^2}{2} v_{xzz} + U' + hU'' \right), \\ \tau_{22} &= -P - hP' - \frac{h^2}{2} P'' - p - hp' - \frac{h^2}{2} p'' + T_{22} + hT_{22}' + \frac{h^2}{2} T_{22}'' \\ &\quad + \left( \frac{\beta_i}{R_1} \right) \left( \frac{\mu_i}{\mu_1} \right) 2 \left( v_z + hv_{zz} + \frac{h^2}{2} v_{zzz} \right). \end{aligned} \tag{A.6}$$

Shear stress balance yields

$$[-h_x \tau_{11} + (1 - h_x^2) \tau_{12} + h_x \tau_{22}] = 0. \tag{A.7}$$

The dimensional normal stress condition is

$$[[\mathbf{n} \cdot \underline{\tau}^* \cdot \mathbf{n}]] = \frac{S^* (\partial^2 h^* / \partial x^{*2})}{[1 + (\partial h^* / \partial x^*)^2]^{3/2}}, \tag{A.8}$$

where  $S^*$  is the surface tension coefficient. In dimensionless form, this is

$$[[\mathbf{n} \cdot \underline{\tau}^* \cdot \mathbf{n}]] = \frac{T}{mR_1} \frac{h_{xx}}{[1 + h_x^2]^{3/2}}, \tag{A.8a}$$

where the dimensionless interfacial tension parameter is  $T = S^*/(\mu_2 U_i)$ . The normal stress condition is  $[[h_x^2 \tau_{11} - 2h_x \tau_{12} + \tau_{22}]] = T/mR_1(h_{xx}/\sqrt{1+h_x^2})$ . The dimensionless equation of motion is

$$\frac{\partial \mathbf{u}}{\partial t} + \mathbf{u} \cdot \nabla \mathbf{u} = \frac{\rho_1}{\rho_i} (\nabla \cdot \mathbf{T} - \nabla p) - F^{-2} \mathbf{e}_z + \frac{\beta_i}{R_i} \nabla^2 \mathbf{u}, \quad (\text{A.9})$$

where the stress tensor is

$$\underline{\tau} = -p\mathbf{I} + \mathbf{T} + \left(\frac{\beta_i}{R_1}\right) \left(\frac{\mu_i}{\mu_1}\right) [\nabla \mathbf{u} + (\nabla \mathbf{u})^T], \quad (\text{A.10})$$

$\mathbf{T}$  is the extra stress tensor. The dimensionless constitutive law for the Oldroyd-B fluid is

$$\mathbf{T} + W_i \frac{D\mathbf{T}}{Dt} = \left(\frac{\mu_i}{\mu_1 R_1}\right) (1 - \beta_i) (\nabla \mathbf{u} + (\nabla \mathbf{u})^T), \quad \mathbf{u} = (u, v), \quad (\text{A.11})$$

where  $D/Dt$  is the upper convected time derivative

$$\frac{D\mathbf{T}}{Dt} = \frac{\partial \mathbf{T}}{\partial t} + (\mathbf{u} \cdot \nabla) \mathbf{T} - (\nabla \mathbf{u}) \mathbf{T} - \mathbf{T} (\nabla \mathbf{u})^T. \quad (\text{A.12})$$

At the interface, the velocity and tangential stress are continuous, the jump in the normal stress is balanced by surface tension and curvature, and the kinematic free surface condition holds.

The dimensionless basic velocity  $(U(z), 0)$  is the same as the Newtonian case:

$$U(z) = \begin{cases} -GR_1 z^2/2 + c_1 z, & 0 \leq z \leq l_1, \\ -rGR_2(z-1)^2/2 + c_2(z-1) + U_p, & l_1 \leq z \leq 1, \end{cases} \quad (\text{A.13})$$

where

$$c_1 = (1 + GR_1 l_1^2/2)/l_1, \quad l_2 = 1 - l_1, \quad c_2 = m(-GR_1 + c_1), \quad (\text{A.14})$$

and the upper plate speed  $U_p$  is

$$U_p = 1 + \frac{ml_2}{l_1} - \frac{GR_1 ml_2}{2}. \quad (\text{A.15})$$

Eq. (A.15) relates  $G$  and  $R_1$ . Here  $mR_1 = rR_2$ . The basic pressure field  $P$  is the same as the Newtonian case and satisfies  $dP/dx = -G$  and

$$\frac{dP}{dz} = \begin{cases} -1/F^2, & 0 \leq z \leq l_1, \\ -1/(rF^2), & l_1 \leq z \leq 1. \end{cases} \quad (\text{A.16})$$

The basic extra stress tensor is

$$\begin{aligned} \underline{\mathbf{T}} &= \begin{pmatrix} C_1 & C_2 \\ C_2 & 0 \end{pmatrix}, \quad C_1 = (1 - \beta_i) \left(\frac{\mu_i}{\mu_1 R_1}\right) 2W_i [U'(z)]^2, \\ C_2 &= (1 - \beta_i) \left(\frac{\mu_i}{\mu_1 R_1}\right) U'(z). \end{aligned} \quad (\text{A.17})$$

Note the basic shear stress condition is  $[[C_2 + (\beta_i/R_1)(\mu_i/\mu_1)U']] = 0$  at  $z = l_1$ . The basic normal stress balance yields  $[[P]] = 0$  at  $z = l_1$ .

Solutions that are perturbations of the above basic flow are sought. The perturbations to the velocity pressure and interface position are denoted by  $(u, v)$ ,  $p$  and  $h$ , respectively. The perturbation to the extra stress tensor is

$$\begin{pmatrix} T_{11} & T_{12} \\ T_{12} & T_{22} \end{pmatrix}. \tag{A.18}$$

The equations of motion in each fluid yield

$$\begin{aligned} \frac{\partial u}{\partial t} + U \frac{\partial u}{\partial x} + vU' + \frac{\rho_1}{\rho_i} \frac{\partial p}{\partial x} - \frac{\rho_1}{\rho_i} \left( \frac{\partial T_{11}}{\partial x} + \frac{\partial T_{12}}{\partial z} \right) - \frac{\beta_i}{R_i} \left( \frac{\partial^2 u}{\partial x^2} + \frac{\partial^2 u}{\partial z^2} \right) &= -u \frac{\partial u}{\partial x} - v \frac{\partial u}{\partial z}, \\ \frac{\partial v}{\partial t} + U \frac{\partial v}{\partial x} + \frac{\rho_1}{\rho_i} \frac{\partial p}{\partial z} - \frac{\rho_1}{\rho_i} \left( \frac{\partial T_{12}}{\partial x} + \frac{\partial T_{22}}{\partial z} \right) - \frac{\beta_i}{R_i} \left( \frac{\partial^2 v}{\partial x^2} + \frac{\partial^2 v}{\partial z^2} \right) &= -u \frac{\partial v}{\partial x} - v \frac{\partial v}{\partial z}. \end{aligned} \tag{A.19}$$

The constitutive equations yield the following coupled equations for the extra stress components:

$$\begin{aligned} T_{11} + W \left( \frac{\partial T_{11}}{\partial t} + U \frac{\partial T_{11}}{\partial x} + vC_1' - 2C_1 \frac{\partial u}{\partial x} - 2C_2 \frac{\partial u}{\partial z} - 2T_{12}U' \right) - (1 - \beta) \left( \frac{2\mu}{\mu_1 R_1} \right) \frac{\partial u}{\partial x} \\ = 2W \left( \frac{\partial u}{\partial x} T_{11} + \frac{\partial u}{\partial z} T_{12} \right) - W \left( u \frac{\partial T_{11}}{\partial x} + v \frac{\partial T_{11}}{\partial z} \right), \end{aligned} \tag{A.20}$$

$$\begin{aligned} T_{12} + W \left( \frac{\partial T_{12}}{\partial t} + U \frac{\partial T_{12}}{\partial x} + vC_2' - C_1 \frac{\partial v}{\partial x} - T_{22}U' \right) - (1 - \beta) \left( \frac{\mu}{\mu_1 R_1} \right) \left( \frac{\partial v}{\partial x} + \frac{\partial u}{\partial z} \right) \\ = W \left( \frac{\partial v}{\partial x} T_{11} + T_{22} \frac{\partial u}{\partial z} \right) - W \left( u \frac{\partial T_{12}}{\partial x} + v \frac{\partial T_{12}}{\partial z} \right), \end{aligned} \tag{A.21}$$

$$\begin{aligned} T_{22} + W \left( \frac{\partial T_{22}}{\partial t} + U \frac{\partial T_{22}}{\partial x} - 2C_2 \frac{\partial v}{\partial x} \right) - (1 - \beta) \left( \frac{2\mu}{\mu_1 R_1} \right) \frac{\partial v}{\partial x} \\ = 2W \left( \frac{\partial v}{\partial x} T_{12} + \frac{\partial v}{\partial z} T_{22} \right) - W \left( u \frac{\partial T_{22}}{\partial x} + v \frac{\partial T_{22}}{\partial z} \right). \end{aligned} \tag{A.22}$$

Incompressibility reads

$$\frac{\partial u}{\partial x} + \frac{\partial v}{\partial z} = 0. \tag{A.23}$$

The boundary conditions are  $u = v = 0$  at  $z = 0, 1$ . The conditions at the interface are posed at  $z = l_1 + h(x, t)$ . Since the unknown  $h(x, t)$  will be assumed to be small, the interfacial conditions are expanded as Taylor series about  $z = l_1$  and yield terms of all orders in the nonlinearity. Thus, we need to decide on the level of truncation for the nonlinearity in the interface conditions. A glance at the final Stuart-Landau Eq. (4) shows that the Landau constant  $\kappa$  is an inner product of the adjoint eigenvector with cubic terms. The  $N_2(\zeta, \chi)$  and  $N_2(\bar{\zeta}, \eta)$  are cubics because they involve products of the eigenfunction with  $\chi$  and  $\eta$  which are quadratic terms, first mentioned in Eq. (2) as stemming from the correction to the solution vector at the quadratic interaction level. The other term in  $\kappa$  is the  $N_3(\zeta, \zeta, \bar{\zeta})$ , the cubic terms in the interface conditions, which we are required to carry for self-consistency to calculate  $\kappa$  to the leading order. For this reason, we express the interface conditions below to the cubic order.

Continuity of velocity yields

$$h \llbracket U' \rrbracket + \llbracket u \rrbracket = -h \left[ \left[ \frac{\partial u}{\partial z} \right] \right] - \frac{h^2}{2} \llbracket U'' \rrbracket - \frac{h^2}{2} \left[ \left[ \frac{\partial^2 u}{\partial z^2} \right] \right], \quad (\text{A.24})$$

$$\llbracket v \rrbracket = -h \left[ \left[ \frac{\partial v}{\partial z} \right] \right] - \frac{h^2}{2} \left[ \left[ \frac{\partial^2 v}{\partial z^2} \right] \right], \quad (\text{A.25})$$

where  $\llbracket x \rrbracket$  denotes  $x$  (fluid 1)– $x$ (fluid 2).

Continuity of shear stress yields

$$\begin{aligned} \llbracket T_{12} \rrbracket - \frac{\partial h}{\partial x} \llbracket C_1 \rrbracket + \left[ \left[ \frac{\beta_i}{R_1} \frac{\mu_i}{\mu_1} (u_z + v_x) \right] \right] &= -h \left[ \left[ \frac{\partial T_{12}}{\partial z} \right] \right] - \frac{\partial h}{\partial x} (\llbracket T_{22} \rrbracket - \llbracket T_{11} \rrbracket) \\ &+ h \frac{\partial h}{\partial x} \left( \llbracket C_1' \rrbracket - \left[ \left[ \frac{\partial T_{22}}{\partial z} \right] \right] + \left[ \left[ \frac{\partial T_{11}}{\partial z} \right] \right] \right) \\ &- \frac{h^2}{2} \left[ \left[ \frac{\partial^2 T_{12}}{\partial z^2} \right] \right] + \frac{h^2}{2} \frac{\partial h}{\partial x} \llbracket C_1'' \rrbracket + \left( \frac{\partial h}{\partial x} \right)^2 \llbracket T_{12} \rrbracket + 2 \frac{\partial h}{\partial x} \left[ \left[ \frac{\beta_i \mu_i}{\mu_1 R_1} \left( -\frac{\partial v}{\partial z} + \frac{\partial u}{\partial z} \right) \right] \right] \\ &- h \left[ \left[ \frac{\beta_i \mu_i}{\mu_1 R_1} \left( \frac{\partial^2 v}{\partial x \partial z} + \frac{\partial^2 u}{\partial z^2} \right) \right] \right] - \frac{h^2}{2} \left[ \left[ \frac{\beta_i \mu_i}{\mu_1 R_1} \left( \frac{\partial^3 v}{\partial x \partial z^2} + \frac{\partial^3 v}{\partial z^3} \right) \right] \right] \\ &+ \left( \frac{\partial h}{\partial x} \right)^2 \left[ \left[ \frac{\beta_i \mu_i}{\mu_1 R_1} \left( \frac{\partial v}{\partial x} + \frac{\partial v}{\partial z} \right) \right] \right] + 2h \frac{\partial h}{\partial x} \left[ \left[ \frac{\beta_i \mu_i}{\mu_1 R_1} \left( -\frac{\partial^2 v}{\partial z^2} + \frac{\partial^2 u}{\partial x \partial z} \right) \right] \right]. \end{aligned} \quad (\text{A.26})$$

Here,  $\llbracket C_2 + (\beta_i/R_1)(\mu_i/\mu_1)U' \rrbracket = 0$ ,  $\llbracket C_2' \rrbracket = G(\beta_1 - \beta_2)$ ,  $\llbracket C_2' + (\beta_i \mu_i/\mu_1 R_1)U'' \rrbracket = 0$ , and  $\llbracket P \rrbracket = 0$  in the basic flow, and  $u_x + v_z = 0$ . The balance of normal stress yields

$$\begin{aligned} \llbracket T_{22} \rrbracket - \llbracket p \rrbracket \frac{T}{m R_1} \frac{\partial^2 h}{\partial x^2} - h \llbracket p' \rrbracket + \left[ \left[ 2 \left( \frac{\beta_i}{R_1} \right) \left( \frac{\mu_i}{\mu_1} \right) v_z \right] \right] \\ = 2 \frac{\partial h}{\partial x} h \left[ \left[ \frac{\partial T_{12}}{\partial z} \right] \right] + 2 \frac{\partial h}{\partial x} \llbracket T_{12} \rrbracket - h \left[ \left[ \frac{\partial T_{22}}{\partial z} - \frac{\partial p}{\partial z} \right] \right] - \left( \frac{\partial h}{\partial x} \right)^2 \llbracket C_1 \rrbracket \\ - \left( \frac{\partial h}{\partial x} \right)^2 \llbracket T_{11} - p \rrbracket - \frac{h^2}{2} \left[ \left[ \frac{\partial^2 T_{22}}{\partial z^2} - \frac{\partial^2 p}{\partial z^2} \right] \right] - \frac{T}{2m R_1} \frac{\partial^2 h}{\partial x^2} \left( \frac{\partial h}{\partial x} \right)^2 \\ + h \left( \frac{\partial h}{\partial x} \right)^2 \llbracket P' - C_1' \rrbracket + 2 \frac{\partial h}{\partial x} \left[ \left[ \frac{\beta_i \mu_i}{\mu_1 R_1} \left( \frac{\partial v}{\partial x} + \frac{\partial u}{\partial z} \right) \right] \right] - 2h \left[ \left[ \frac{\beta_i \mu_i}{\mu_1 R_1} \frac{\partial^2 u}{\partial z^2} \right] \right] \\ - 2 \left( \frac{\partial h}{\partial x} \right)^2 \left[ \left[ \frac{\beta_i \mu_i}{\mu_1 R_1} \frac{\partial u}{\partial x} \right] \right] + 2h \frac{\partial h}{\partial x} \left[ \left[ \frac{\beta_i \mu_i}{\mu_1 R_1} \left( \frac{\partial^2 v}{\partial x \partial z} + \frac{\partial^2 u}{\partial z^2} \right) \right] \right] - h^2 \left[ \left[ \frac{\beta_i \mu_i}{\mu_1 R_1} \frac{\partial^3 u}{\partial z^3} \right] \right]. \end{aligned} \quad (\text{A.27})$$

The kinematic free surface condition yields

$$\frac{\partial h}{\partial t} + U(l_1) \frac{\partial h}{\partial x} - v_1 = -\frac{\partial h}{\partial x} (u_1 + hU_1') + h \frac{\partial v_1}{\partial z} - h \frac{\partial h}{\partial x} \frac{\partial u_1}{\partial z} + \frac{h^2}{2} \frac{\partial^2 v_1}{\partial z^2} - \frac{\partial h}{\partial x} \frac{h^2}{2} U_1'', \quad (\text{A.28})$$

where the subscript 1 here refers to fluid 1.

In the linearized stability analysis,  $u$ ,  $v$ ,  $p$ ,  $T_{ij}$  and  $h$  are proportional to  $\exp(i\alpha x + \sigma t)$ , where  $\sigma$  denotes complex-valued eigenvalues.

### Appendix B. Mean flow component

Since  $\chi$  is not periodic in  $x$ , its component  $v$  satisfies  $dv/dz = 0$  by incompressibility. Since  $v = 0$  at  $z = 0, 1$ ,  $v = 0$  in the entire domain. Denote the quadratic terms on the right hand sides of Eqs. (A.19)–(A.23) in the momentum and constitutive equations as before by  $f_1, \dots, f_{10}$ . Denote the quadratic terms of the right hand sides of Eqs. (A.24)–(A.28) by  $f_{11}$ – $f_{15}$ , respectively. We note that  $f_{15}$  in  $N_2(\zeta, \bar{\zeta})$  vanishes.

We carry out the formulation for  $\chi$  keeping the pressure gradient in the  $x$ -direction fixed in the entire nonlinear analysis. Putting  $d/dx = 0$ ,  $d/dt = 0$ , and  $v = 0$  in the equations of motion, the components in  $\chi$  satisfy:

$$\frac{-\rho_1}{\rho_i} \frac{\partial T_{12}}{\partial z} - \frac{\beta}{R_1} \frac{\partial^2 u}{\partial z^2} = f_1 \text{ or } f_6 \text{ of } N_2(\zeta, \bar{\zeta}), \tag{B.1}$$

$$\frac{\rho_1}{\rho_i} \left( \frac{\partial p}{\partial z} - \frac{\partial T_{22}}{\partial z} \right) = f_2 \text{ or } f_7, \tag{B.2}$$

$$T_{11} + W \left( -2C_2 \frac{\partial u}{\partial z} - 2T_{12}U' \right) = f_3 \text{ or } f_8, \tag{B.3}$$

$$T_{12} - WT_{22}U' - (1 - \beta) \frac{\mu}{\mu_1 R_1} \frac{\partial u}{\partial z} = f_4 \text{ or } f_9, \tag{B.4}$$

$$T_{22} = f_5 \text{ or } f_{10}. \tag{B.5}$$

$$u = 0 \text{ at } z = 0, 1, \tag{B.6}$$

$$h[[U']] + [[u]] = f_{11}, \tag{B.7}$$

$$\left[ \left[ T_{12} + \frac{\beta\mu}{\mu_1 R_1} \frac{\partial u}{\partial z} \right] \right] = f_{13}, \tag{B.8}$$

$$[[T_{22} - p]] - h[[P']] = f_{14}. \tag{B.9}$$

To preserve the given volumes of the fluids, we set  $h = 0$  for  $\chi$ . To fully determine  $p$  requires an additional condition: we set  $p$  for fluid 1 equal to zero at  $z = l_1$ . The problem for the pressure decouples:

$$\frac{\partial p}{\partial z} = \frac{\partial f_5}{\partial z} + f_2 \text{ in fluid 1,} \tag{B.10}$$

$$\frac{\partial p}{\partial z} = \frac{\partial f_{10}}{\partial z} + \frac{1}{r} f_7 \text{ in fluid 2,} \tag{B.11}$$

$$[[p]] = [f_5]_{z=l_1} - [f_{10}]_{z=l_1} - f_{14}, \quad p_2(l_1) = 0. \tag{B.12}$$

The problem for  $u$  and  $T_{12}$  consists of Eqs. (B.1), (B.4), (B.6)–(B.8).  $T_{11}$  is then calculated from Eq. (B.3).

## References

- [1] K.C. Su, B. Khomami, An experimental/theoretical investigation of interfacial instabilities in superposed pressure-driven channel flow of well-characterized viscoelastic fluids. Part I: linear stability and encapsulation effects, *J. Non-Newt. Fluid Mech.*, Submitted for publication.
- [2] D.D. Joseph, Y.Y. Renardy, *Fundamentals of Two-Fluid Dynamics. Part I: Mathematical Theory and Applications. Part II: Lubricated Pipelining, Drops and Miscible Liquids*, Springer, New York, 1993.
- [3] Y. Renardy, Weakly nonlinear behavior of periodic disturbances in two-layer Couette-Poiseuille flow, *Phys. Fluids*. A1 (1989) 1666.
- [4] Y. Renardy, Weakly nonlinear behavior of periodic disturbances in two-layer plane channel flow of upper-convected Maxwell liquids, *J. Non-Newt. Fluid Mech.* 56 (1995) 101.
- [5] A.V. Coward, Y. Renardy, Thin film core-annular flow of upper-convected Maxwell liquids, *J. Non-Newt. Fluid Mech.* 70 (1997) 155.
- [6] P.J. Blennerhassett, On the generation of waves by wind, *Phil. Trans. R. Soc. London A298* (1980) 451.
- [7] A.V. Coward, Y. Renardy, M. Renardy, J.R. Richards, Temporal evolution of periodic disturbances in two-layer Couette flow, *J. Comp. Phys.* 132 (1997) 346.
- [8] J. Li, Y. Renardy, M. Renardy, A numerical study of periodic disturbances on two-layer Couette flow, *Phys. Fluids* 10 (1998) 3056.
- [9] J. Li, Y. Renardy, Direct simulation of unsteady axisymmetric core-annular flow with high viscosity ratio, *J. Fluid Mech.* (1999) in press.
- [10] G.M. Wilson, B. Khomami, An experimental investigation of interfacial instabilities in multilayer flow of viscoelastic fluids. Part I. Incompatible polymer systems, *J. Non-Newt. Fluid Mech.* 45 (1992) 355.
- [11] G.M. Wilson, B. Khomami, An experimental investigation of interfacial instabilities in multilayer flow of viscoelastic fluids. Part II. Elastic and nonlinear effect in incompatible polymer systems, *J. Rheol.* 37 (2) (1993) 315.
- [12] M.M. Ranjbaran, B. Khomami, The effect of interfacial instabilities on the strength of the interface in two-layer plastic structures, *Polym. Eng. Sci.* 36 (1996) 1875.
- [13] Y.-Y. Su, B. Khomami, Interfacial stability of multilayer viscoelastic fluids in slit and converging channel die geometries, *J. Rheol.* 36 (1992) 357.
- [14] Y.-Y. Su, B. Khomami, Purely elastic interfacial instabilities in superposed flow of polymeric fluids, *Rheol. Acta* 31 (1992) 413.
- [15] R. Sureshkumar, A.N. Beris, Linear stability analysis of viscoelastic poiseuille flows using Arnoldi-based orthogonalization algorithm, *J. Non-Newt. Fluid Mech.* 95 (1995) 151.
- [16] Y. Renardy, Stability of the interface in two-layer Couette flow of upper convected Maxwell liquids, *J. Non-Newt. Fluid Mech.* 28 (1988) 99.
- [17] K. Chen, D.D. Joseph, Elastic shortwave instability in extrusion flows of viscoelastic liquids, *J. Non-Newt. Fluid Mech.* 42 (1992) 189.
- [18] K. Chen, Interfacial instabilities in stratified shear flows involving multiple viscous and viscoelastic fluids, *Appl. Mech. Rev.* 48(11) part 1 (1995) 763.
- [19] Y. Renardy, An instability of plane Couette flow of the Johnson-Segalman liquid, in: Y. Renardy, A.V. Coward, D. Papageorgiou, S.M. Sun (Eds.), *Advances in Multi-Fluid Flows*, Society for Industrial and Applied Mathematics, Philadelphia, 1996, p. 199.
- [20] M. Renardy, Y. Renardy, Derivation of amplitude equations and analysis of sideband instabilities in two-layer flows, *Phys. Fluids A5* (1993) 2738.